PAPER • OPEN ACCESS

Effects of surface hardening by laser shock peening and shot peening on a nickel-based single-crystal superalloy CMSX-4

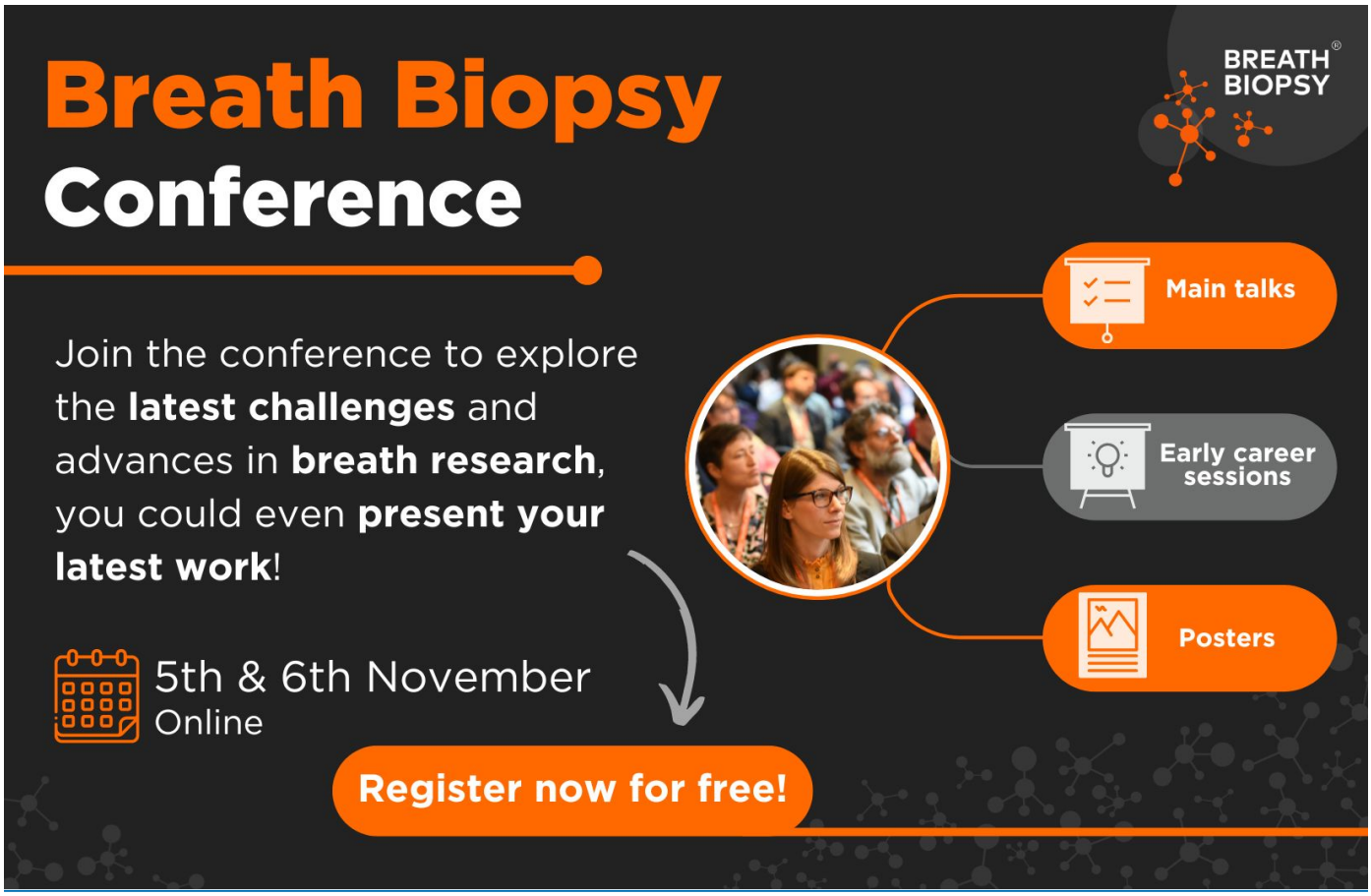

Materials Research Express

PAPER

Effects of surface hardening by laser shock peening and shot peening on a nickel-based single-crystal superalloy CMSX-4

Aabid Husen Hakeem[1], **Nicolau I Morar**[2], **Karl Dawson**[3], **Gordon J Tatlock**[3], **Grant J Gibson**[4] and **Simon Gray**[1]

[1] Cranfield University, Bedfordshire, MK43 0AL, United Kingdom
[2] City, University of London, London, EC1V 0HB, United Kingdom
[3] University of Liverpool, Liverpool, L69 3BX United Kingdom
[4] Rolls-Royce plc, PO Box 31, Derby, DE24 8BJ, United Kingdom

E-mail: a.hakeem@cranfield.ac.uk

Keywords: work hardening, microhardness, laser shock peening, shot peening, nickel single-crystal

OPEN ACCESS

RECEIVED
28 February 2024

REVISED
8 July 2024

ACCEPTED FOR PUBLICATION
18 July 2024

PUBLISHED
31 July 2024

Abstract

Improving the expected life of nickel-based single-crystal superalloy turbine components by surface hardening treatments including laser shock peening (LSP) and mechanical shot peening (MSP) are of particular interest for mitigation of life limiting damage such as environmental assisted cracking in hot section components of gas turbines. In the present study the effects of LSP and MSP on the surface roughness, microhardness and work hardening of a nickel-based single crystal superalloy CMSX-4® have been assessed. Surface roughness was measured using laser profilometry. The degree of work hardening was measured using electron backscattered diffraction with local misorientation analysis. The analysis showed evidence for a work hardening layer in the MSP sample to a depth of approximately 70 μm. Sets of slip bands extending far into the bulk of the sample were observed in the LSP-treated sample, without any evidence of a work hardening layer. Microhardness measurements used to gauge the depth of residual stress showed that LSP produced a much deeper hardness profile than MSP, with compressive residual stress depths of 1000 μm and 200 μm in LSP and MSP respectively. The retention of hardness after a heat treatment of 50 h at 700 °C was more prominent in the LSP sample than in the MSP sample. LSP and MSP have therefore been shown to be at the opposite ends of the spectrum of surface hardening treatments of CMSX-4, with LSP giving milder hardening, but to a greater depth.

1. Introduction

Nickel-based single-crystal superalloys are known for their high resistance to creep, thermal fatigue and oxidation, making them ideal materials for turbine blades in the hot section of gas turbine engines [1, 2]. As a result of an industry drive for improved efficiency, modern gas turbine engines are increasingly spending longer times at temperatures. The airframes have also predominantly moved towards twin engine aircraft as a result of a combination of drivers, simplicity of product portfolio, the increased reliability of modern engines and the multi-mode operation that many airline operators increasingly desire. When combined, these factors increase the susceptibility to environmentally assisted attack, which can result in customer disruption. Whilst historically it has been known that sulphidation a relatively recent discovery has observed environmental attack at temperatures below the traditional sulphidation limit of 600 °C [2–4].

Surface hardening treatments such as laser shock peening (LSP) have been successfully employed elsewhere in the aerospace, defence, marine, power generation and automotive sectors to mitigate fatigue cracking and stress corrosion cracking (SCC) damage [5–7]. LSP is considered to be a more controllable and flexible, providing a deeper compressive residual stress (CRS) and a cleaner alternative to mechanical shot peening (MSP) [8]. By comparison, MSP has been the most widely used surface hardening technique historically due to low cost, ease of implementation and inexpensive maintenance [9]. In MSP, small spherical hard shots are fired at high

Table 1. Chemical composition of CMSX-4®.

Composition	Cr	Co	Mo	Al	Ti	Ta	W	Hf	Re	Ni
Weight %	6.5	9.0	0.6	5.6	1.0	6.5	6.0	0.1	3.0	Bal.

velocity on the sample surface to introduce plastic deformation and compressive residual stresses, thereby improving the fatigue resistance of materials [10, 11]. Both surface hardening techniques have been applied to a wide range of alloys and ceramics [12]. However, in comparison with other materials, the surface hardening of Ni-based single-crystal superalloys has received relatively little attention, both in LSP [13–21] and in MSP [22, 23]. Further understanding of their effect on the surface properties, cold work and performance of these superalloys is still required.

Surface CRSs are known to relax at high temperatures [24–26], while work hardening has been shown to be retained at high temperatures [27, 28]. Another factor impacting fatigue cracking and environmentally assisted damage is the surface roughness, as irregular features as peaks and valleys on the sample surface tend to trap corrosive agents and may act as crack nucleation sites [29–31]. The effect of a surface hardening treatment on the sample surface roughness must therefore also be considered when evaluating the effectiveness of a given treatment.

In-depth hardness profiles obtained from microhardness measurements can be used to estimate the depth of CRS and work hardening in a sample. Surface residual stresses generated in polycrystalline samples by surface hardening techniques are traditionally measured either by x-ray diffraction (XRD), using the $\sin^2\psi$ method [32, 33], or by centre hole drilling [34]. The latter involves the measurement of the locally relieved strain by placing a strain gauge rosette around a hole drilled in the sample surface, and taking its readings as the drilled-out depth is increased incrementally [35]. However, both the XRD $\sin^2\psi$ method and centre hole drilling analysis usually rely on the assumption that the sample's elastic properties are isotropic. This assumption is justified for polycrystalline materials, but manifestly not for a nickel-based single-crystal superalloy, the stiffness of which varies substantially with crystallographic orientation [36]. The Ortner method [37, 38], an XRD-based alternative for measuring CRS in single crystal materials, is complex and extremely time-consuming. It has been shown that microhardness profiles correlate well with the depth of compressive residual stress in previous studies on as-treated shot peened alloys [39, 40], and can also be used to indicate the depth of the work hardened layer. Therefore, microhardness profiles can provide guidance to the depth of CRS and work hardening during the assessment of surface hardened single-crystal superalloys.

In the present study, the effects of LSP and MSP on the surface and sub-surface properties of a Ni-based single crystal superalloy CMSX-4® are investigated. The surface roughness, microhardness profile, the structure and depth of the work hardened layer were characterised in samples treated either by LSP or MSP. The key differences between the as-treated states induced by both surface hardening treatments are identified and discussed.

2. Experimental details

2.1. Sample preparation

The material investigated in this paper is a widespread nickel-based single crystal superalloy, CMSX-4. The chemical composition of the alloy is shown in table 1.

The microstructure of CMSX-4 consists of a minority disordered gamma (γ) matrix phase, with dispersed cuboid gamma prime (γ') precipitates constituting most of the volume. Cylindrical bars of as-cast CMSX-4 were cut by wire-electrical discharge machining to produce samples of 58 mm long, 6 mm wide and 4 mm thick, with $\langle 001 \rangle$ crystallographic orientations lying along the length of each sample. The secondary crystallographic orientations normal to the surface hardened faces were uncontrolled. Subsequent analysis showed that MSP and LSP samples, investigated using electron microscopy, had secondary orientations approximately parallel to $\langle 100 \rangle$ and $\langle 310 \rangle$, respectively. Such variations in secondary orientation have previously been shown to have only a minor effect on the cold working of CMSX-4 [34].

A total of 5 samples were produced for this study. Thermal stress relieving was performed on all samples after machining at 900 °C for 2 h in vacuum, following which samples were cleaned in an ultrasonic bath with isopropyl alcohol for 10 min. Two sets of two samples each were then treated either by LSP or MSP under identical conditions, specified in sections 2.2.1 and 2.2.2, respectively. One sample was left bare, without any surface hardening, for control purposes. A LSP and a MSP sample were further subjected to a heat treatment of 50 h at 700 °C to assess the effect of thermal exposure on the microhardness profiles of the samples.

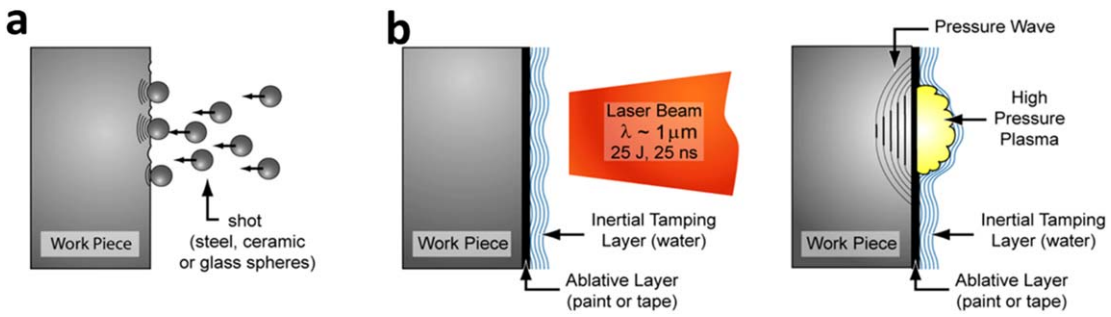

Figure 1. Schematic representation of (a) MSP and (b) LSP surface treatment. Courtesy of curtiss-wright surface technologies (copyright).

2.2. Surface hardening treatments

2.2.1. Laser shock peening

LSP without an ablative coating as represented in figure 1 was performed on two of the samples. LSP involves pulsing the surface of the workpiece with a high intensity laser beam, which generates an expanding high-pressure plasma with aid of a confined water layer. The impact of the plasma upon the surface of the workpiece creates shockwaves which travel through the material. When the amplitude of the shock wave is greater than the Hugoniot elastic limit, the dynamic yield strength, the material is plastically deformed [41]. The magnitude of this plastic deformation decreases with distance from the peened surface, as the amplitude of shockwave also decreases. Deformation ceases when the amplitude of the shock wave falls below the Hugoniot elastic limit [42].

In this study, LSP was performed at Cranfield University using a bespoke Nd: Glass 535 nm laser with a power density of 7 GW cm^{-2}, a circle spot size of 600 μm, and a pulse duration of 10 ns. Two scans per sample were performed, with travelling speed of 70 mm s^{-1} and overlap of 85%. The LSP parameters were chosen based on prior work, which established this set of values as resulting in an optimal sample state [43].

2.2.2. Mechanical shot peening

MSP was performed by Metal Improvement Company Curtis-Wright Surface Technologies UK. Two samples were peened with 4–6 A intensity, cast steel 230H (H signifying hard cast steel shot) and 200% coverage. Peening intensity is an indirect measure of the process power, and is dependent on the nozzle pressure, nozzle angle, shot velocity, and shot material and size. Shot type specifies the size of the peening media used, in thousandths of inch, and its material. Coverage is the percentage of the surface to have been impacted, with coverages above 100% signifying a proportionately longer peening time. The MSP parameters chosen in this study are representative of those used in industrial applications and have been shown to give a good combination of properties in polycrystalline samples [28].

Prior to MSP and LSP treatment, the surface of the samples was polished, removing approximately 10 μm of the material surface to get rid of any white layers induced by machining.

2.3. Characterisation

2.3.1. Surface roughness

Characterisation of surface roughness in the LSP and MSP samples was performed using a *Talysurf 120L* surface scanning profilometer. Three individual line scans were performed on each sample with a 0.88 mm scan path to ensure accuracy of the roughness values obtained. The parameters R_a, R_q and R_z were used to quantify surface roughness. R_a is the average deviation of the surface profile from its mean line. It is the most widely considered surface parameter and is defined in equation (1-1) [44].

$$R_a = L^{-1} \int_0^L y(x)\,dx \tag{1-1}$$

where x is the distance along the surface, y(x) defines the height of the surface profile relative to the mean line, and L is the sampling length.

R_q or the root mean square (RMS) roughness is equal to one standard deviation of the profile about the mean line. R_q is defined in equation (1-2) [44].

$$R_q = (L^{-1} \int_0^L y^2(x)\,dx)^{0.5} \tag{1-2}$$

R_z is the maximum peak to valley height of the profile within the sampling height.

2.3.2. Electron microscopy

Imaging and analysis of sample microstructures was undertaken using an electron backscatter channelling contrast images (EBSCCI) were recorded using a Zeiss Gemini field emission gun (FEG) scanning electron microscope (SEM) SEM 450. SEM images were recorded using a range of beam energies: 5 kV to 20 kV acceleration voltage, beam currents between 1 and 10nA and a fixed position backscattered electron (BSE) detector. Conditions were optimised for channelling contrast, where BSE yields, hence signal intensity and contrast is extremely sensitive to crystal orientation. This effect is known as orientation contrast, channelling contrast, or crystallographic contrast [44] and in extreme circumstances, the technique is sufficiently sensitive to enable imaging of individual dislocations and crystal defects, including stacking faults, slip bands and mechanically induced nano-twinning [45].

Electron backscattered diffraction (EBSD) was used to probe the structure of cold work through the sample depth away from the worked surface. EBSD data, giving the crystallographic orientation of the material in each scan pixel, was recorded with the sample tilted 70° using an Oxford Instruments Symmetry detector and Aztec acquisition software, with a scan step size of 0.5 μm. EBSD data was filtered, deleting any pixels with fewer than three indexed nearest neighbours, in order to remove noise from the sample surfaces. Following the acquisition of EBSD data, local misorientation (LM) analysis was performed to obtain maps of cold work within the sample. LM analysis takes advantage of the fact that in a cold worked layer, some of the generated dislocations form into networks with non-zero net Burgers vectors (geometrically necessary dislocations), thereby creating small local differences in the material crystallographic orientation [45, 46]. The amount of local misorientation can be quantified by calculating the kernel average neighbour misorientation (KANM) parameter for each pixel in an EBSD dataset. KANM takes the value of the average difference in crystallographic orientation between the given pixel and its neighbours within an n×n grid (the kernel) around it [47]. Greater dislocation density results in larger values of KANM, which allows KANM to be used as a measure of local cold work.

Using a self-written Python-based script, KANM values were calculated for each pixel in the EBSD datasets, using a 3×3 kernel and a 2° exclusion angle, meaning any misorientations greater than 2° were excluded to avoid potential effects of defects or recrystallisation [47]. KANM values were then plotted as colour maps to showcase the distribution of work hardening in the treated surface cross-sections. The averages and standard deviations of KANM values in each scan line were plotted against depth from the surface to obtain profiles of cold work in each sample. The depth of cold work was calculated as the depth at which the average KANM value in a given profile fell below a baseline, defined as the 100 smallest (average + one standard deviation) KANM values in a scan.

Further, electron transparent TEM samples were prepared in a FEI Helios 600i NanoLab Ga focussed ion beam (FIB) dual beam instrument. Site specific specimens were sectioned from regions of material approximately 35 μm beneath the peened surface of both the MSP and LSP samples. Lamellae were produced by the lift out method [48, 49], and each received a low energy, 5 kV final surface finish, to minimise the effects of Ga ion beam induced damage. Bright field, scanning transmission electron microscope (BF-STEM) images were recorded using a probe aberration corrected JEOL 2100FCs S/TEM microscope, operating at 200 kV. Contrast in BF-STEM images results predominantly from mass thickness and diffraction contrast. Hence, in single crystal CMSX-4 alloy, contrast arises primarily from the difference in density between γ and γ' phases, and from diffraction contrast caused by dislocations and stacking faults.

2.3.3. Microhardness

A Zwick/Roell Indentec was employed to measure sample Vickers microhardness profiles in depth, perpendicular to $\langle 001 \rangle$. For each sample, five rows of 15 indents each were made with an applied load of 500 g and 15 s dwell time, starting from the surface to a depth of 2000 μm. The mean and standard deviation of microhardness for each depth was calculated to obtain the hardness value and a measure of error for that depth. The indents were spaced according to the ASTM standard for Vickers microhardness tests.

3. Results and discussion

3.1. Surface roughness

The values of the surface roughness parameters—R_a, R_q, R_z—for the bare, LSP and MSP samples are shown in table 2. As expected, the bare specimen showed the smoothest surface, with an average roughness (R_a) of 0.011 μm, root mean square value (R_q) of 0.021 μm and a maximum roughness depth (R_z) of 0.088 μm. As shown below, these values are considerably lower than the corresponding values for the treated samples.

An increased roughness was observed in the LSP sample, with $R_a = 1.116$ μm, $R_q = 1.683$ μm and $R_z = 15.186$ μm. This is in accordance with previous studies, which have reported an increase in the surface roughness after LSP [37, 44]and is due to the high energy plasma being generated during LSP, which alters the

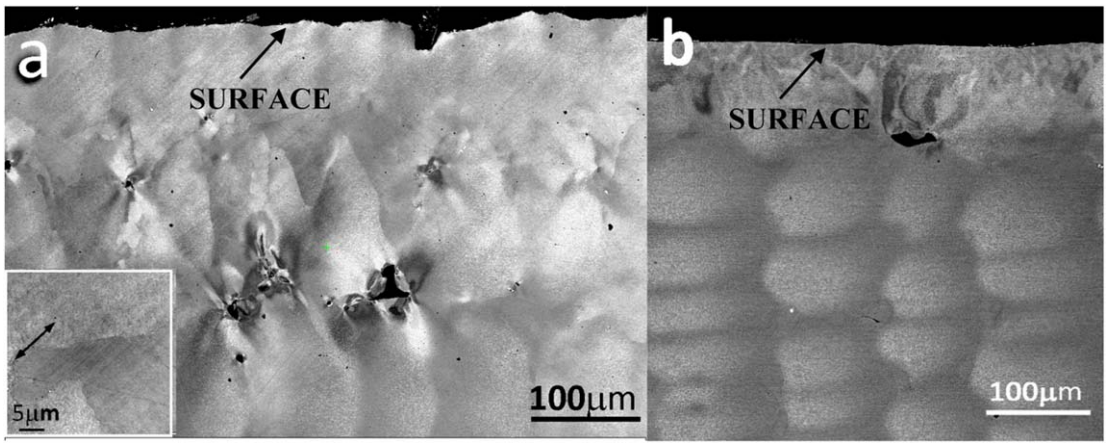

Figure 2. Electron channelling contrast orientation images showing (a), deformation in LSP material surrounding voids and slip bands in the eutectic phase, the direction indicated by arrow (inset) and (b), deformation in MSP material, to a depth of approximately 100 μm. Bands of light and dark in the bulk of both samples show residual dendritic segregation from the casting process.

Table 2. Surface roughness for the bare, LSP and MSP samples.

Parameter	Bare	LSP	MSP
R_a (μm)	0.011	1.116	0.262
R_q (μm)	0.021	1.683	0.332
R_z (μm)	0.088	15.186	1.083

surface, creating a much rougher surface compared to bare CMSX-4. The MSP sample is seen to have a much smoother surface, with lower values of R_a, R_q and R_z when compared to the LSP sample, as was expected from the pre-testing polishing performed.

3.2. Work hardening

Secondary electron images of the LSP and MSP samples, shown in figure 2, offer a ready comparison between the two treated samples. The microstructure of single crystal CMSX-4 alloy, sectioned close to a $\langle 001 \rangle$ crystallographic orientation, consists of a cube shaped γ' precipitate distribution in a γ matrix network. However, there are also inhomogeneities, including solidification shrinkage pores and areas of eutectic phase. In general, shrinkage pores are near spherical in shape and this was observed in material unaffected by MSP and LSP processing. However, orientation contrast images showing near surface areas of laser shock peened alloy, to depths greater than 750 μm, revealed image contrast surrounding voids, that indicate a significant amount of plastic deformation (figure 2(a)). Similar distortion was also observed in MSP material, but to a depth not greater than 100 μm (figure 2(b)); in contrast, these features were not observed in areas of material unaffected by peening. Furthermore, numerous series of parallel features, running approximately 45° to the sample surface normal and more pronounced in eutectic regions, were observed in the LSP sample (figure 2(a) inset). The trace of $\{111\}$ slip band faults lie in the $\langle 011 \rangle$ crystallographic directions, hence it is argued that these features are in fact observed due orientation contrast resulting from the presence of slip bands. Slip bands were also evidenced in orientation contrast images of MSP material, again, only to depths less than 100 μm. No evidence was recorded of either slip bands, or plastic deformation surrounding solidification pores, in material unaffected by peening processes, hence it is reasoned that these features were not an artifact of sample preparation.

Bright field STEM images revealed a typical microstructure, comprised of comparatively dense, hence dark, γ channels surrounding brighter cube shaped γ' precipitates. On occasion, areas of γ, in the plane of the thin lamellae were captured. These relatively dark expanses of images can be seen toward the top right corner of figure 3(a), and the lower left corner of figure 3(b).

LSP processed CMSX-4 alloy is shown in figure 3(a). Short dislocation lines can be seen in both γ and γ' phases, although the dislocation density appears greater in the γ channels. Many of the deformation features, residing in the γ' precipitates were $\{111\}$ stacking faults lying approximately parallel to $\langle 011 \rangle$ crystallographic slipping directions, whereas the direction of dislocations in the γ phase was less ordered.

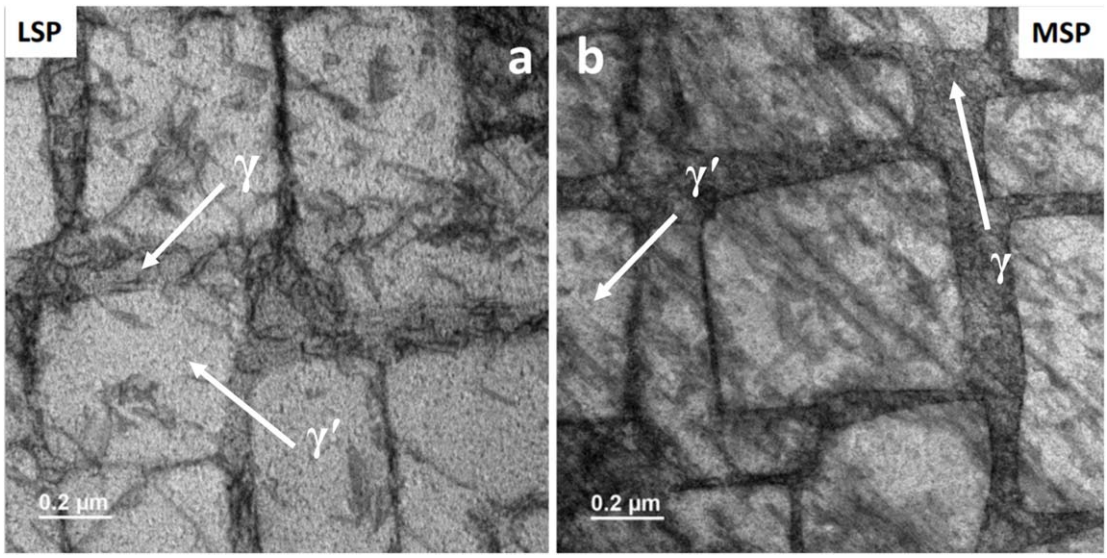

Figure 3. BF-STEM images showing dislocation and slip band distributions in γ and γ' regions of (a), LSP and (b), MSP processed CMSX-4 alloy.

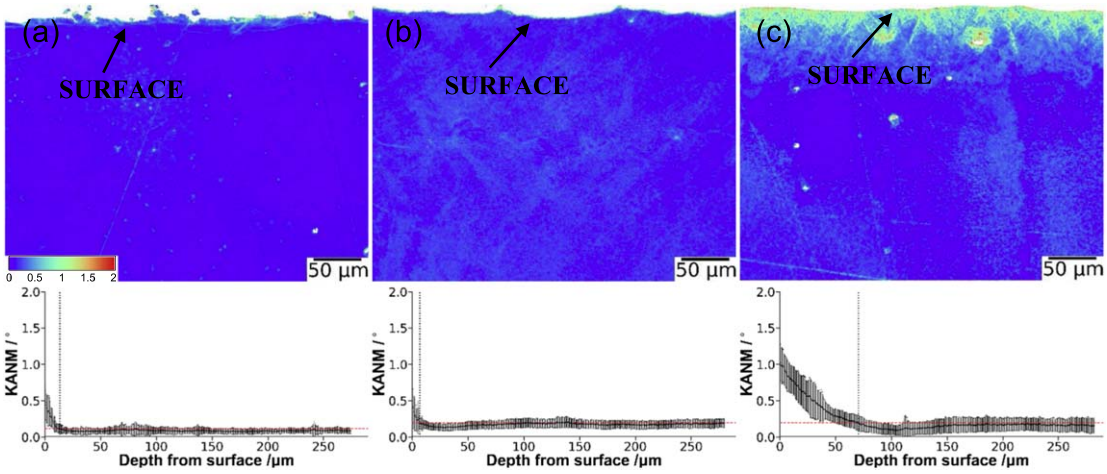

Figure 4. Maps of KANM values and corresponding depth profiles of the (a) bare, (b) LSP and (c) SP samples. The red horizontal lines in the profiles indicate the baseline value for each map. Black dashed vertical lines indicate the position of the profile 'depth'. Bright straight lines, particularly in (a) and (c) are scratches.

Crystal deformation was also observed in the MSP specimen (figure 3(b)). Stacking faults and dislocations were observed, {111} stacking faults being ubiquitous throughout the γ' precipitates; dislocations were concentrated in the γ matrix. In contrast to the LSP sample, deformation in the γ' phase showed a preferred single $\langle 011 \rangle$ orientation variant. This observation is consistent with SEM observations, where slip bands were seen to adopt a preferred orientation, over large expanses of material.

In comparison with the global differences in material orientation revealed by secondary electron imaging, KANM maps represent the local material misorientation, directly dependent on local dislocation density rather than the relative movement of different sections of the sample. KANM maps and profiles of the bare, LSP and MSP samples are shown in figure 4. Except at the sample surface, where misorientation is high due to the effects of sample machining, and in some isolated artefacts caused by scratching or porosity, the bare sample shows an entirely uniform KANM map, and a flat KANM profile figure 4(a), indicating that there are no areas of increased dislocation density, as expected.

Similarly to the bare sample, the KANM map of the LSP sample figure 4(b), shows a slight rise in KANM at the surface, followed by a largely uniform map, with no evidence of significant bulk cold work. Previous studies on LSP of polycrystalline samples have observed generally low levels of cold work, with concentrations of

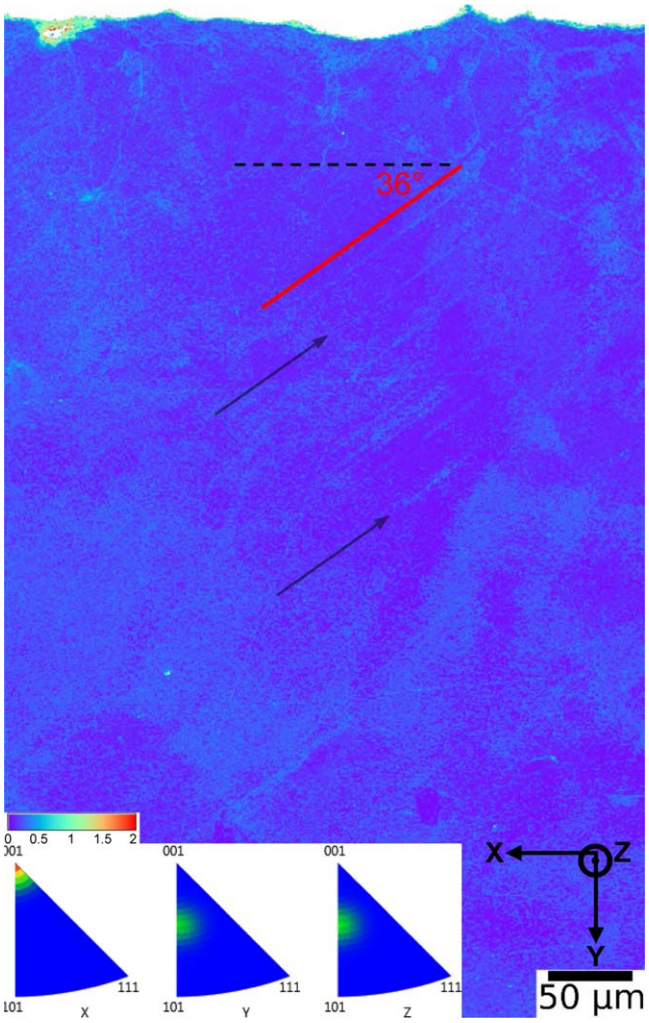

Figure 5. KANM map of the LSP sample up to 600 μm depth from the surface, with inverse pole figures showing the average crystallographic orientation of the material relative to the sample X, Y and Z axes as defined in the figure. X, Y and Z are approximately parallel to [1 0 0], [21 8 1] and [18 7 1] respectively. A number of slip bands are observed in the middle of the map, select ones indicated by grey arrows. Slip bands all lie at approximately 36° to the horizontal, as shown by the red line in the figure.

dislocation density near grain boundaries [49, 50]. The complete absence of significant levels of bulk cold work in single crystal samples is very interesting. The surface increase in LM is attributable to either machining damage, or a small layer of nanorecrystallisation, seen in literature to occur at LSP surfaces [51].

On the other hand, the MSP sample possesses a clear surface layer of bulk increased dislocation density, seen as a region of high KANM values in figure 4(c), coinciding with the layer of contrast seen in figure 4(b). KANM values are greatest at the surface of the sample, with line averages of 1.0°, decreasing monotonously to a flat baseline of 0.2°. The depth of cold work for the MSP sample is measured as 71 μm, and when the 10 μm of depth lost to polishing is added to this value, it is consistent with previous work on the dependence of MSP cold work depth on shot peening intensity [22].

Once again, a bulk layer of substantial cold work is observed in the MSP sample, but not in the LSP sample, which appears very similar to the bare sample. The absence of bulk cold work is particularly interesting in light of the significant increase in the material microhardness following LSP, particularly within 300 μm of the sample surface (see section 3.3)—precisely the region where no bulk cold work is observed. This reinforces the notion that the increase in microhardness can be correlated with the induced CRS.

However, a number of distinctive parallel line features are observed in the LSP sample. These can be seen in figure , as well as throughout figure 4(b). The lines, although faint, are frequent and recur at a constant angle of approximately 36° to the horizontal. This angle is consistent with the traces of the {111} slip planes in CMSX-4 possessing the greatest resolved shear stress for the given sample crystallographic orientation (figure 5, bottom), assuming a uniaxial normal stress perpendicular to the sample surface. The line features are therefore most likely to be slip bands. The presence and frequency of these slip bands shows that local plastic deformation, as opposed

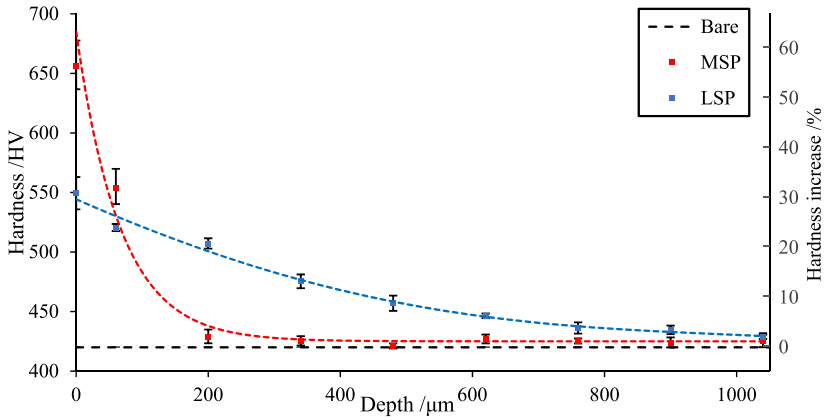

Figure 6. The variation of microhardness with depth in the MSP and LSP samples. An average value for bare CMSX-4 is given as a baseline. The vertical axis on the right shows the corresponding percentage increase in hardness above the bare CMSX-4 baseline.

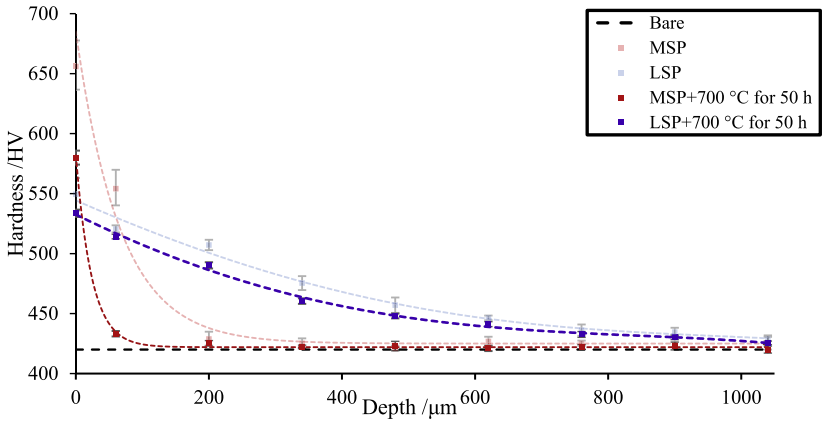

Figure 7. The variation of microhardness with depth in the LSP and MSP samples after thermal exposure of 700 °C for 50 h. Profiles for un-heat-treated MSP and LSP samples are plotted for comparison. An average value for bare CMSX-4 is given as a baseline.

to a bulk increase in dislocation density, is still occurring during LSP, and is likely the mechanism by which the compressive residual stress is generated.

3.3. Microhardness

The cross-sectional microhardness of the LSP, MSP and bare CMSX-4 was studied in order to analyse the variation of microhardness with depth from the sample surface. It was found that the average microhardness value of the bare sample is approximately 420 HV, and this value was taken as the point of reference to compare the improvement in microhardness of the peened samples. Microhardness profiles of the MSP and LSP samples are given in figure 6.

As can be seen from figure 6, MSP produced a greater hardening at the sample surface than LSP, with microhardness increased to a maximum of 656 HV in the MSP sample, versus 549 HV in LSP, in comparison with an average value of 420 HV for bare CMSX-4. It was also observed that the LSP sample shows a much more gradual gradient of microhardness compared to the MSP sample. The overall hardened depths are approximately 1000 and 200 μm for the LSP and MSP samples respectively, suggesting a much greater depth of CRS in the LSP sample.

There is some evidence that the percentage increase in microhardness correlates with the percentage of sample cold work [52]. If this measure is used, then it can be seen from figure 6 that substantial cold work (10%) is present in the LSP sample up to about 500 μm, but only up to around 130 μm in the MSP sample.

To investigate the thermal stability of the increased microhardness, an LSP and an MSP sample were heat treated for 50 h at 700 °C. As shown in figure 7, following the thermal exposure, the LSP sample retains its increased hardness to a greater depth when compared to MSP, even though both samples show substantial decreases in hardness. The MSP sample still displays the highest surface hardness, but this reduces drastically at around 50 μm, and almost reaches the reference value after 100 μm. The decrease in hardness following heat

treatment is less pronounced in the LSP sample. Reduction of the peened material hardness can be explained by dislocation rearrangement at the high temperature conditions, which results in CRS relaxation. The much smaller cold work generated by LSP when compared to MSP therefore most likely lead to the smaller CRS relaxation observed.

4. Conclusions

The fatigue life and resistance to SCC of surface hardened samples is dependent on the cumulative effect of surface roughness, compressive residual stress and degree of cold work. In this paper, a comprehensive comparison of these parameters between samples of a nickel-based single crystal superalloy CMSX-4, subjected to LSP or MSP under optimal processing conditions, has been made. The following conclusions can be derived:

- The sample subjected to LSP showed a significant increase in roughness when compared to the as-cast bare sample, in accordance with previous studies [53, 54]. The surface roughness of the MSP sample, greater than that of the bare sample, showed a significant decrease compared to the LSP. This does not comply with previous literature, which reports that samples subjected to MSP have a much rougher surface compared to LSP samples [54]. This anomaly can be explained by the fact that before being provided for this study, the MSP samples were polished, creating a much smoother surface.
- The results reported also show that the microhardness of surface hardened samples (both LSP and MSP) increased considerably compared to bare CMSX-4. The MSP sample had the highest value of hardness on the surface, which decreased rapidly down to 200 μm. Samples subjected to LSP showed greater retention in depth of the hardened layer up to 1000 μm. Following a thermal exposure of 700 °C for 50 h, both MSP and LSP showed a decrease in hardness values. Hardness loss was less pronounced in LSP than in MSP, likely as a result of much less cold work induced in the LSP sample.
- A significant difference between LSP and MSP was seen in the results of the electron microscopy. Little or no cold work was detected in the surface of the LSP sample, in constrast with the MSP sample, which possessed a clear surface layer of increased material misorientation to a depth of 71 μm. Interestingly, this shows that the increase in microhardness observed in the LSP sample must be attributable to the compressive residual stress within the sample surface.
- Slip band traces were seen throughout the depth of the LSP sample, indicating that the sample had undergone some localised plastic deformation, which is required in order for residual stresses to be present.

This study has established clear differences between the as-processed states of single crystal superalloy samples subjected to LSP and MSP, and has demonstrated the efficacy of the EBSD KANM analysis method when comparing these two techniques on a single crystal sample. Subsequent investigations of the corrosion fatigue behaviour of this material will aim to establish how the observed properties—the differences in surface roughness, depth and thermal stability of the residual stresses, and the degree of cold working—influence the material fagitue life.

Acknowledgments

The authors would like to thank the Engineering and Physical Science Research Council for financial support of the research work (Grant number EP/ I033246/1) and Rolls-Royce Plc for providing the bare material, for their technical support and useful discussions. We would also like to acknowledge the support provided by Welding Engineering and Laser Processing Centre, Cranfield with laser shock peening, and the Metal Improvement Company, Derby with the shot peening of the samples. Lastly, Ivan Bogachev and Kevin M Knowles from Cambridge University for supporting the EBSD KANM analysis.

Data availability statement

All data that support the findings of this study are included within the article (and any supplementary files).

Declaration of competing interest

The authors declare that they have no known competing financial interests or personal relationships that could have appeared to influence the work reported in this paper.

ORCID iDs

Aabid Husen Hakeem https://orcid.org/0009-0002-7125-9768
Nicolau I Morar https://orcid.org/0000-0001-9109-8864

References

[1] Okazaki M and Sakaguchi M 2008 Thermo-mechanical fatigue failure of a single crystal Ni-based superalloy *Int. J. Fatigue* **30** 318–23
[2] Brooking L, Sumner J, Gray S and Simms N J 2018 Stress corrosion of Ni-based superalloys *Mater. High Temp.* **3409** 120–9
[3] Chapman N, Gray S, Sumner J and Nicholls J 2021 Stress corrosion testing of CMSX-4, CM247LC DS and IN6203DS Ni-base superalloys *Oxid. Met.* **95** 85–104
[4] Brandal G and Lawrence Yao Y 2016 Material Influence on mitigation of stress corrosion cracking via laser shock peening *J. Manuf. Sci. Eng.* **139** 011002
[5] Hackel L, Rankin J, Racanellia T, Mills T and Campbell J H 2015 Laser peening to improve fatigue strength and lifetime of critical components *Procedia Eng.* **133** 545–55
[6] Ganesh P *et al* 2012 Studies on laser peening of spring steel for automotive applications *Opt. Lasers Eng.* **50** 678–86
[7] Rankin L, Truong J, Dane C, Harris C B and Hackel F 2009 Laser peening to mitigate stress corrosion cracking of nuclear power facilities *Can. Nucl. Soc. - 30th Annu. Can. Nucl. Soc. Conf. 33rd CNS/CNA Student Conf.* 2009, 148–56 (https://osti.gov/etdeweb/biblio/21256473) accessed May 25, 2021
[8] Hammersley G, Hackel L A and Harris F 2000 Surface prestressing to improve fatigue strength of components by laser shot peening *Opt. Lasers Eng.* **34** 327–37
[9] Kirk D 1999 Shot peening *Aircr. Eng. Aerosp. Technol.* **71** 349–61
[10] Morançais A, Févre M, Kanoute P, Kruch S and François M 2014 Impact of residual stresses on the fatigue behavior of a Nickel-based superalloy *Mater. Sci. Forum* (Trans Tech Publications Ltd) 747–54
[11] Chen Y H and Jiang C H 2013 Effect of shot peening on surface characteristics of ni-based single-crystal superalloy *Mater. Trans.* **54** 1894–7
[12] Gujba A K and Medraj M 2014 Laser peening process and its impact on materials properties in comparison with shot peening and ultrasonic impact peening *Materials* **7** 7925–74
[13] Lu G X, Liu J D, Qiao H C, Zhou Y Z, Jin T, Zhao J B, Sun X F and Hu Z Q 2017 Surface nano-hardness and microstructure of a single crystal nickel base superalloy after laser shock peening *Opt. Laser Technol.* **91** 116–9
[14] Tang Z, Wang K, Geng Y, Dong X, Duan W, Sun X and Mei X 2021 An investigation of the effect of warm laser shock peening on the surface modifications of [001]-oriented DD6 superalloy *Int. J. Adv. Manuf. Technol.* **113** 1973–88
[15] Tang Z, Wang K, Dong X, Duan W and Mei X 2021 Effect of warm laser shock peening on the low-cycle fatigue behavior of DD6 nickel-based single-crystal superalloy *J. Mater. Eng. Perform.* **30** 2930–9
[16] Kattoura M, Mannava S R, Qian D and Vasudevan V K 2017 Effect of laser shock peening on elevated temperature residual stress, microstructure and fatigue behavior of ATI 718Plus alloy *Int. J. Fatigue* **104** 366–78
[17] Rozmus-Górnikowska M, Kusiński J, Cieniek Ł and Morgiel J 2021 The microstructure and properties of laser shock peened CMSX4 superalloy *Metall. Mater. Trans.*A **52** 2845–58
[18] Geng Y, Mo Y, Zheng H, Li G and Wang K 2021 Effect of laser shock peening on the hot corrosion behavior of Ni-based single-crystal superalloy at 750 °C *Corros. Sci.* **193** 109419 Effect of laser shock peening on the hot corrosion behavior of Ni-based single-crystal superalloy at 750°C
[19] Chen L, Sun Y, Li L and Ren X 2020 Microstructural evolution and mechanical properties of selective laser melted a nickel-based superalloy after post treatment *Mater. Sci. Eng.* A **792** 139649
[20] Cao J, Cao X, Jiang B, Yuan F, Yao D and Huang J 2021 Microstructural evolution in the cross section of Ni-based superalloy induced by high power laser shock processing *Opt. Laser Technol.* **141** 107127
[21] Morar N I, Holtham N, Hackel L, Davami K, Sharma M, DeWald A and Roy R 2023 Effects of high-energy laser peening followed by pre-hot corrosion on stress relaxation, microhardness, and fatigue life and strength of single-crystal nickel CMSX-4® superalloy *Int. J. Adv. Manuf. Technol.* **126** 4893–912
[22] Bogachev I, Knowles K M and Gibson G J 2020 Electron backscattered diffraction analysis of cold work in a shot peened single crystal nickel superalloy *Materialia* **14** 100860
[23] Morançais A, Fèvre M, François M, Kanouté P, Kruch S and Longuet A 2014 Impact of shot-peening on a single crystal nickel-based superalloy *Adv. Mater. Res.* (Trans Tech Publications Ltd) 70–5
[24] Messé O M D M, Stekovic S, Hardy M C and Rae C M F 2014 Characterization of plastic deformation induced by shot-peening in a Ni-Base superalloy *JOM* **66** 2502–15
[25] Clauer A H and Lahrman D F 2001 Laser shock processing as a surface enhancement process *Key Eng. Mater.* **197** 121–44
[26] Buchanan D J and John R 2014 Residual stress redistribution in shot peened samples subject to mechanical loading *Mater. Sci. Eng.*A **615** 70–8
[27] Foss B J, Gray S, Hardy M C, Stekovic S, McPhail D S and Shollock B A 2013 Analysis of shot-peening and residual stress relaxation in the nickel-based superalloy RR1000 *Acta Mater.* **61** 2548–59
[28] Chin K S, Idapalapati S and Ardi D T 2020 Thermal stress relaxation in shot peened and laser peened nickel-based superalloy *J. Mater. Sci. Technol.* **59** 100–6
[29] Hoffmeister J, Schulze V, Wanner A, Hessert R and Koenig G 2008 Thermal relaxation of residual stresses induced by shot peening in IN718 *10th Int. Conf. Shot Peen* 1–6 (http://mtu.de/en/technologies/engineering_news/production/Koenig_Thermal_relaxation.pdf)

[30] Cockings H L, Cockings B J, Harrison W, Dowd M, Perkins K M, Whittaker M T and Gibson G J 2020 The effect of near-surface plastic deformation on the hot corrosion and high temperature corrosion-fatigue response of a nickel-based superalloy *J. Alloys Compd.* **832** 154889
[31] Evans A, Kim S B, Shackleton J, Bruno G, Preuss M and Withers P J 2005 Relaxation of residual stress in shot peened Udimet 720Li under high temperature isothermal fatigue *in: Int. J. Fatigue* (Elsevier BV) 1530–4
[32] Cullity B D and Stock S R 2001 *Elements of X-Ray Diffraction* 3rd edn (Prentice-Hall)
[33] Morançais A, Fèvre M, François M, Guel N, Kruch S, Kanouté P and Longuet A 2015 Residual stress determination in a shot-peened nickel-based single-crystal superalloy using x-ray diffraction *J. Appl. Crystallogr.* **48** 1761–76
[34] Schajer G S and Whitehead P S 2018 Hole-drilling method for measuring residual stresses *Synth. SEM Lect. Exp. Mech.* **10** 1–186
[35] Rossini N S, Dassisti M, Benyounis K Y and Olabi A G 2012 Methods of measuring residual stresses in components *Mater. Des.* **35** 572–88
[36] Reed R C 2006 *The Superalloys: Fundamentals and Applications* (Cambridge University Press) (https://doi.org/10.1017/CBO9780511541285)
[37] Ortner B 1985 The choice of lattice planes in x-ray strain measurements of single crystals *Adv. X-Ray Anal.* **29** 113–8
[38] Kanouté P, Morançais A, Longuet A, François M, Fèvre M, Guel N and Kruch S 2015 Residual stress determination in a shot-peened nickel-based single-crystal superalloy using x-ray diffraction *J. Appl. Crystallogr.* **48** 1761–76
[39] Tosha K 2002 Influence of residual stresses on the hardness number in the affected layer produced by shot peening *2nd Asia-Pacific Forum Precis. Surf. Mach. Deburring Technol* (https://researchgate.net/publication/242632054_Influence_of_Residual_Stresses_on_the_Hardness_Number_in_the_Affected_Layer_Produced_by_Shot_Peening) (accessed May 25, 2021)
[40] Maleki E, Unal O and Reza Kashyzadeh K 2019 Efficiency analysis of shot peening parameters on variations of hardness, grain size and residual stress via taguchi approach *Met. Mater. Int.* **25** 1436–47
[41] Sano Y, Mukai N and Obata M 2008 Laser peening without coating : process , effects and applications *Proc. 10th Int. Conf. Shot Peen.* (http://shotpeening.org/ICSP/icsp-10.php)
[42] Peyre P and Fabbro R 1995 Laser shock processing: a review of the physics and applications *Opt. Quantum Electron.* **27** 1213–29
[43] Hakeem A H 2019 *Effect of Laser Shock Peening on the Mechanical Behaviour of CMSX-4 Single Crystal Nickel-based Superalloy* (Cranfield University)
[44] Prior D J *et al* 1999 The application of electron backscatter diffraction and orientation contrast imaging in the SEM to textural problems in rocks *Am. Mineral.* **84** 1741–59
[45] Gutierrez-Urrutia I, Zaefferer S and Raabe D 2013 Coupling of electron channeling with EBSD: toward the quantitative characterization of deformation structures in the sem *JOM* **65** 1229–36
[46] Ashby M F 1970 The deformation of plastically non-homogeneous materials *Philos. Mag. A J. Theor. Exp. Appl. Phys.* **21** 399–424
[47] Ruggles T J, Fullwood D T and Kysar J W 2016 Resolving geometrically necessary dislocation density onto individual dislocation types using EBSD-based continuum dislocation microscopy *Int. J. Plast.* **76** 231–43
[48] Wright S I, Nowell M M and Field D P 2011 A review of strain analysis using electron backscatter diffraction *Microsc. Microanal.* **17** 316–29
[49] Giannuzzi L A and Stevie F A 1999 A review of focused ion beam milling techniques for TEM specimen preparation *Micron* **30** 197–204
[50] Hu X, Yang Y, Zhao J, Lu Y, Wu J and Qiao H 2021 Surface integrity evolution of a Ni-based single crystal superalloy by laser shock peening *Appl. Surf. Sci. Adv.* **6** 100183
[51] Gill A S, Telang A, Ye C, Mannava S R, Qian D and Vasudevan V K 2018 Localized plastic deformation and hardening in laser shock peened inconel alloy 718SPF *Mater. Charact.* **142** 15–26
[52] Zhou L, Long C, He W, Tian L and Jia W 2018 Improvement of high-temperature fatigue performance in the nickel-based alloy by LSP-induced surface nanocrystallization *J. Alloys Compd.* **744** 156–64
[53] Kudryavtsev Y V I V and Rymynova 1961 The Increasing Hardness of Steels as a Result of cold working *Mech. Prop.* **3** 444–7
[54] Karthik D and Swaroop S 2017 Laser shock peening enhanced corrosion properties in a nickel based Inconel 600 superalloy *J. Alloys Compd.* **694** 1309–19